Fuel 315 (2022) 123201

Contents lists available at ScienceDirect

Fuel

journal homepage: www.elsevier.com/locate/fuel

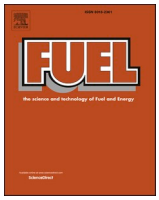

Full Length Article

A multi-generation system for hydrogen production through the high-temperature solid oxide electrolyzer integrated to 150 MW coal-fired steam boiler

Oguz Arslan [a,*], Emin Acikkalp [b], Gamze Genc [c]

[a] Mechanical Engineering Department, Engineering Faculty, Bilecik Seyh Edebali University, Bilecik, Turkey
[b] Mechanical Engineering Department, Engineering Faculty, Eskisehir Technical University, Eskisehir, Turkey
[c] Mechanical Energy Systems Engineering Department, Engineering Faculty, Erciyes University, Kayseri, Turkey

ARTICLE INFO

Keywords:
Coal-fired boiler
Enriched air combustion
Exergy
High-temperature solid oxide electrolyzer
Supercritical ORC
Waste heat

ABSTRACT

A multi-generation system including power generation, domestic hot water, and H_2 production was designed for the waste recovery of a 150 MW coal-fired power plant. A high-temperature electrolyzer was integrated into the present system to produce H_2. The second product of O_2 from the electrolyzer was used to enrich the combustion process. The required power for the electrolyzer was obtained from a bottoming organic Rankine cycle (ORC). In this regard, a supercritical ORC was designed in which cyclopentane was used as the working fluid. The required heat of the electrolyzer was obtained by a heat exchanger located in the combustion chamber to reach the required temperature level. The designed system was analyzed by the energy and exergy method for different temperatures and current densities. It is determined that it is available to produce H_2 in an amount of 0.0739 to 0.0762 kmol/s for the optimal current densities at every single handled temperature. The energy efficiency of the overall system was determined in the range of 27.19% and 27.36%. The exergy efficiency of the overall system was determined in the range of 35.05% and 35.25%. An increase of 15.78–16.53% in energy efficiency was achieved. This increase was achieved as 20.43–21.16% in the exergy efficiency.

1. Introduction

There are many ways to improve the effectiveness of a coal-fired boiler. The common ways are to improve the preheating combustion technology [1-3], to improve the quality of the fuel by dewatering process [4-6], or to use both [7-9]. Besides, the challenging way is to increase the oxygen (O_2) amount of the air to obtain oxy-enriched combustion (OEC) and oxy-fuel combustion for the higher efficient combustion process [10-12]. In this aim, the production of O_2 is the most critical issue to be taken into consideration. Two standard methods, namely distillation, and adsorption are usually used to obtain pure O_2. The electrolysis of water is also a beneficial method to obtain O_2 since it also produces a valuable fuel of H_2.

In comparison to other methods, electrolysis is more expensive since it needs an external heat and electricity source. However, electrolysis can be a more attractive solution when a free source supplies external energy. Renewable energy sources such as solar [13], wind [14], geothermal [15], or a hybrid of these [16,17] are widely used in this way.

The use of waste heat is another effective way to obtain free energy for the electrolyzer unit. Proton exchange membrane electrolyzer (PEMEL), aided by waste heat, is profitable for H_2 production [18-21]. In the previous study of the author(s) which investigates the O_2 and H_2 production by the waste flue gases and its effects, it is conducted that the integration of PEMEL to the coal-fired power plant increases the overall efficiency as well as the boiler efficiency [22]. Feili et al. [20]. Designed a novel trigeneration system including power generation, cooling, and H_2 production. The power generation was obtained by an ORC with zeotropic mixtures, where cooling was obtained by the ejector refrigeration cycle, and H_2 was produced by PEMEL. The maximum exergy efficiency was reported as 42.46%, with an approximately H_2 production of 20 kg/h. Shaofu et al. [23] investigated a multi-generation energy system coupled with a CO_2 capture unit fed by the waste energy of a typical industrial factory. In the study, they integrated a PEMEL into the system resulting in H_2 production of 0.0085 kg/s. The highest exergy efficiency was reported as 43%. Jamali and Noorpoor [24] investigated a multi-generation system including cooling, H_2 production, and power

* Corresponding author.
E-mail address: oguz.arslan@bilecik.edu.tr (O. Arslan).

https://doi.org/10.1016/j.fuel.2022.123201
Received 18 November 2021; Received in revised form 6 January 2022; Accepted 9 January 2022
Available online 17 January 2022

Nomenclature

D	molecular or Knudsen diffusion coefficient
D^{eff}	effective diffusion coefficient
$\dot{E}$	energy rate (kW)
ex	specific flow exergy (kJ/kg)
$\dot{E}x$	exergy rate (kW)
F	Faraday's constant
G	Gibbs energy (kJ)
h	specific enthalpy (kJ/kg)
$\bar{h}$	specific molar enthalpy (kJ/mole)
I	exergy destruction rate (kW)
J	current density (A/m^2)
J_0	exchange current density (A/m^2)
$\dot{m}$	mass rate (kg/s)
$\dot{n}$	molar rate (kmole/s)
P	Pressure (kPa, bar, or atm)
$\dot{Q}$	heat rate (kW)
r	pore diameter (m)
R	universal gas constant (kJ/mole K)
s	specific entropy (kW/kgK)
T	temperature (K or ^{o}C)
V	Voltage (V)
$\dot{W}$	work rate (kW)
x	molar fraction
y	exergy destruction ratio

Greek symbols

γ	pre-exponential coefficient (A/m^2)
δ	Thickness (m)
ε	exergy efficiency (%), Lennard–Jones length, porosity
ζ	tortuosity
η	energy efficiency (%)
κ	Boltzmann's constant
λ	coefficient of excess air
σ	collusion diameter (m)
τ	electrical conductivity (1/Ωm)
Ω	diffusion collision integral

Subscripts

a	anode
act	activation
c	cathode
cc	combustion chamber
d	destruction
f	fuel
g	generated
i	inlet or ith component
k	kth component
K	Knudsen diffusion
l	anode or cathode
o	outlet
ohm	ohmic
p	product or reactant
s	isentropic
T	value at a specified temperature
0	value at the reference state

Superscripts

ch	chemical
f	formation
I	interface
ph	physical
Q	exergy term related to heat
W	exergy term related to work
o	standard or inlet condition

Abbreviations

ALL	alkaline electrolyzer
APH	air pre-heater
B	boiler
C	compressor
CB	compressor block
Con	condenser
GWP	global warming potential
HB	HTEL block
HE	heat exchanger
HTEL	high-temperature electrolyzer
LSM	$La_{1-x}Sr_xMnO_3$
M	mixing chamber
OB	ORC block
TOP	ozone deplation potentail
ORC	organic Rankine cycle
P	pump
T/G	Turbine-generator group
YES	Yttria Stabilized Zirconia

generation. The system was fed by the waste heat of the cement plant and aided by solar energy. In the H_2 production process, PEMEL was used. It was reported in the study that it was available to produce 11.2 kg/h of H_2. Since a high-temperature solid oxide electrolyzer (HTEL) needs relatively less power but more thermal energy, it is more suitable to use an HTEL to evaluate the waste heat [25,26]. Zhao et al. [27] investigated H_2 production by HTEL. The external heat integration was evaluated for different temperature scales in the study. The indicated that internal heat generation was not sufficient to heat feedstock. The study reported that 16% of the required power could be reduced by using external heat sources. In the literature, limited studies are available on this topic, esp. on the waste heat of stack gases. Seyitoglu et al. [28] investigated H_2 production by coal gasification. They handled the HTEL system fed by the Brayton cycle, the steam Rankine cycle (SRC), the organic Rankine cycle (ORC). They reported the energy and exergy efficiency of the system as 41% and 36.5%, respectively. The reported H_2 production changes between 1.7 and 2.4 kg/s for the handled different coal types. Wang et al. [29] investigated the performance of HTEL integrated into a marine diesel engine. The HTEL was fed by the steam generated using the waste heat of the engine exhaust gases. The lacking heat energy for the steam generation was obtained by an electrical heater. The electrical power was obtained from an ORC plant integrated into the system. They conducted an H_2 production of 0.431 kg/s. Toklu et al. [30] investigated the HTEL performance fed by steam generated using the stack gases of an undefined furnace. They indicated it was possible to produce H_2 up to 18 kg/h. Kowalczyk et al. [31] investigated the H_2 production through an HTEL fed by a high-temperature nuclear reactor waste. They reported an H_2 production of 4392 kg/h and a decrease of 26 % of nominal electric power where the energy efficiency was increased from 50.59% to 55.83% by integrating HTEL. Balta et al. [32] designed an HTEL system fed by the waste of the Brayton cycle, conventional Rankine cycle, and ORC. They reported an H_2 production of 0.057 kg/s with an energy efficiency of 87% and exergy efficiency of 88% in the HTEL. Mehrpooya et al. [33] developed a new integrated process including power, heat, and H_2 production. The system was fed by the waste heat of the combustor. They used HTEL for H_2 production. In the study, the production of H_2 was reported as 2.823 kg/h with the trigeneration system efficiency of 71.55%. Ishaq et al.

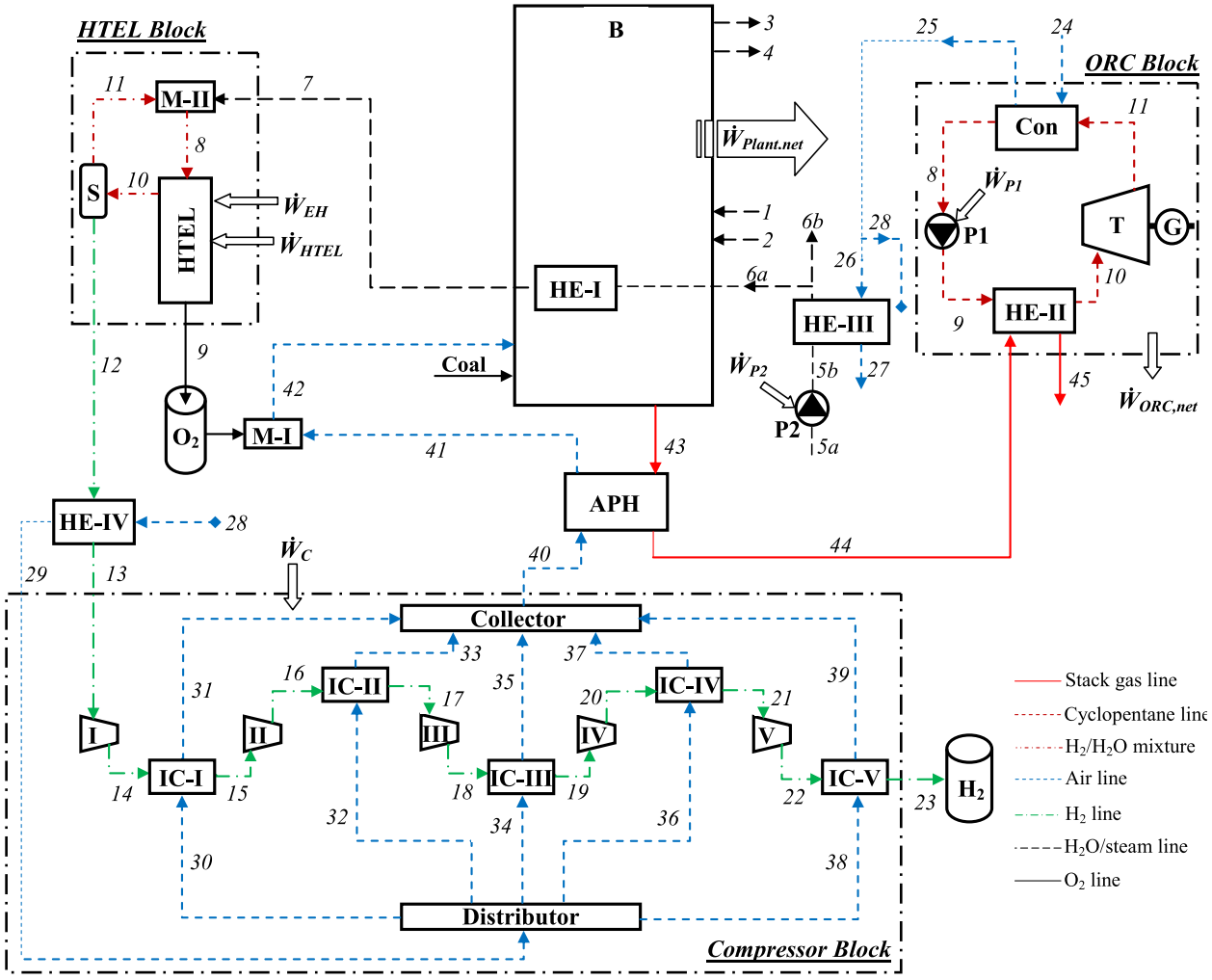

Fig. 1. Flow diagram of the designed multi-generation system.

[34] proposed a new clean H_2 production system fed by the waste heat of cement slag. The new multi-generation system was formed of an electrolysis unit, power generation (reheat Rankine) cycle, and hydrolysis unit. H_2 was produced by the Cu-Cu cycle. They reported that it was available to produce 19.6 mol/s of H_2 with an exergy efficiency of 31.8%. Wang et al. [35] conducted a thermodynamic analysis for H2 production by HTEL fed by engine waste heat. They reported that it was available to produce 22.39 kg/h oh H2 with an electrical efficiency of 85.17% for HTEL. Zhang et al. [36] investigated the integration of HTEL into methanol production fed by biomass (sawdust). Two different models were handled in the system, including full conversion of carbon and zero power exchange. Adding HTEL to biomass to the methanol system made the system efficiency increase up to 13%. Hosseini [37] investigated H_2 production by an integrated system including gas turbine and HTEL. In the system, biogas was used as fuel in the gas turbine, and the waste heat of the gas turbine was used in HTEL. The study reported that the increasing temperature of steam made the H_2 production drastically increase.

The conventional lignite-fired power plants are commonly based on retro designs in which the energy losses are incredibly high. New additional structures can still recover these losses. From this point of view, the improvement of the combustion in the boiler and the additional power generation by bottoming ORC and H_2 production for energy harvesting seem like the possible integration systems. This study conducted a new multi-generation system design for H_2 production by integrating an HTEL system to a 150 MW coal-fired power plant. The designed system was evaluated by the energy and exergy method to measure the performance and find the optimum working conditions. The novelty of this study lies in the two main aspects: First, an HTEL was modeled in a higher sensitivity. The model was compared with the data in the literature and showed more agreeable outputs with the experimental literature. Second, the HTEL was integrated into a coal-fired boiler system. So, the required heat was obtained from the boiler. The electrolysis product of O_2 was used to enrich the combustion. So, the boiler's combustion efficiency was increased, and the required fuel was decreased. The other electrolysis product of H_2 was stored as an energy output of the system. The required electricity was obtained from a bottoming organic Rankine cycle powered by the waste heat of the boiler. Finally, all the processes mentioned above were combined in a new design of a multi-generation system, including power, H_2 as an energy harvesting material, domestic heat, in conjunction with the increased boiler efficiency.

2. System description

The novel system was designed to recover the waste heat of the stack gases of the Seyitomer coal-fired power plant. The handled unit has an air preheating system with an output temperature of stack gases ranging between 285 and 305 °C [38,39]. Since there is still a large amount of energy, a multi-generation system was considered. The multi-generation system includes an HTEL block to produce H_2, an ORC block to generate electricity for the HTEL, and a compressor block to store produced H_2.

Table 1
The characteristic values of the existing boiler system.

Points		T (°C)	P (kPa)	$\dot{m}$ (kg/s)
H_2O	1	493.15	15,730.90	131.90
	2	622.15	3,432.00	120.50
	3	811.15	13,729.00	131.90
___	4	811.15	3,383.00	120.50
Coal		–	–	75.13

The flowchart of the designed system is given in Fig. 1.

The present boiler (B) was designed to evaluate the pulverized lignites with low-calory. It includes the superheater, re-heater, economizer, and air pre-heater (APH). A heat exchanger (HE-I) is located in the boiler's combustion chamber to obtain the required high-temperature (points 6 and 7) steam for the HTEL for the multi-generation system. In the new design, the main structure of the boiler system is protected. So, the output values (points 1 to 4) and the net power generation ($\dot{W}_{Plant,net}$) do not change for the whole plant except for the mass ratios. The corresponding values of the existing boiler system are given in Table 1.

The used heat in the boiler for HTEL steam will affect the mass ratio in the same amount. This issue will be included in evaluations of the overall system. The stack gases are first in APH for the final heating of combustion air (points 41–44), later sent to the ORC block.

The required power is obtained from an ORC power block fed by the waste heat of the stack gases. ORC is designed as the supercritical cycle, including four main components, namely condenser (Con), pump (P1), turbine-generator group (T/G), and evaporator (HE-II). Cyclopentane is used in the cycle as the working fluid since it is the most appropriate refrigerant depending on the working conditions [40]. The cooling in the condenser is made by the air (points 24 and 25), which some part (point 28) is later used in the combustion process, and the other part (point 26) is used for the preheating of HTEL steam in the heat exchanger (HE-III).

HTEL block consists of a separator, a mixing unit, and the main electrolyzer structure. HTEL is designed as the cathode-supported type and consists of an anode layer (LSM–YSZ), a cathode layer (Ni–YSZ), an electrolyte layer (YSZ), and two interconnect layers including fuel and sweeping O_2 channels. Pure H_2 is obtained by separating process (point 12), where the remained H_2-H_2O concoction (point 11) is sent to the mixing unit (M−II). This concoction is mixed with the high-temperature steam (point 7) from the boiler to form the primary feeding fuel of the electrolyzer (point 8). If the heat generated by the HTEL is not sufficient, the needed part is considered to be obtained from an electrical heater ($\dot{W}_{EL}$). Pure H_2 is sent to the compressor block (point 13) for the storage process after it gives its heat energy to the combustion air in the heat exchanger (HE-IV), where the produced O_2 is sent to a mixer to form the enriched combustion air (point 9).

The compressor block is formed in five stages to decrease the required power. The heat generated in the block is recovered to heat the combustion air. In this regard, the H_2 is compressed throughout points 13 to 23, where the combustion air is heated throughout points 29 to 40.

3. Thermodynamic analysis

The newly designed system is evaluated by exergy analysis in conjunction with the continuity of mass and the first law of thermodynamics. The mass, energy, and exergy balance equations for the steady-state conditions are orderly given as follows:

$$\sum \dot{m}_i - \sum \dot{m}_o = 0 \tag{1}$$

$$\dot{Q} - \dot{W} + \sum \dot{m}_i h_i - \sum \dot{m}_o h_o = 0 \tag{2}$$

$$\dot{E}x_{d,k} = \dot{E}x_k^Q - \dot{E}x_k^W - \sum \left(\dot{m}_i ex_i\right)_k - \sum \left(\dot{m}_o ex_o\right)_k \tag{3}$$

where $\dot{Q}$ is heat rate term, $\dot{W}$ is work term, $\dot{m}$ is the mass rate. i indicates the inlet conditions and o indicates the outlet conditions.$\dot{E}x_{d,k}$, $\dot{E}x_k^Q$, $\dot{E}x_k^W$ and ex respectively describe the destructed exergy, the exergy of heat energy, the exergy of work and the specific exergy of flow, and are given as[41]:

$$\dot{E}x_k^Q = \left(1 - \frac{T_0}{T}\right)\dot{Q}_k \tag{4}$$

$$\dot{E}x_k^W = \dot{W}_k \tag{5}$$

$$ex_i = ex_i^{Ph} + ex_i^{Ch} \tag{6}$$

where ex_k^{ph} is the physical exergy term and is given by Eq. (7) or (8):

$$ex_i^{Ph} = (h_i - h_0) - T_0(s_i - s_0) \tag{7}$$

Table 2
Energy and exergy balances of the multi-purposed system.

Compound	Energy balances	Exergy balances
B	$\dot{Q}_f - \dot{Q}_B + \dot{m}_1 h_1 + \dot{m}_2 h_2 + \dot{m}_{6a} h_{6a} - \dot{m}_3 h_3 - \dot{m}_4 h_4 - \dot{m}_7 h_7 = 0$	$\dot{E}x_f - \dot{E}x_B^Q + \dot{m}_1 ex_1 + \dot{m}_2 ex_2 + \dot{m}_{6a} ex_{6a} - \dot{m}_3 ex_3 - \dot{m}_4 ex_4 - \dot{m}_7 ex_7 = \dot{E}x_{d,B}$
APH	$\dot{m}_{40} h_{40} + \dot{m}_{43} h_{43} - \dot{m}_{41} h_{41} - \dot{m}_{44} h_{44} = \dot{Q}_{APH}$	$\dot{m}_{40} ex_{40} + \dot{m}_{43} ex_{43} - \dot{m}_{41} ex_{41} - \dot{m}_{44} ex_{44} - \dot{E}x_{APH}^Q = \dot{E}x_{d,APH}$
HE-I	$\dot{m}_{6a} h_{6a} - \dot{m}_7 h_7 + \dot{Q}_{f,HE-I} = 0$	$\dot{m}_{6a} ex_{6a} - \dot{m}_7 ex_7 + \dot{E}x_{f,HE-I}^Q = \dot{E}x_{d,HE-I}$
HE-III	$\dot{m}_5 h_5 + \dot{m}_{26} h_{26} - \dot{m}_{6a} h_{6a} - \dot{m}_{6b} h_{6b} - \dot{m}_{27} h_{27} = \dot{Q}_{HE-III}$	$\dot{m}_5 ex_5 + \dot{m}_{26} ex_{26} - \dot{m}_{6a} ex_{6a} - \dot{m}_{6b} ex_{6b} - \dot{m}_{27} ex_{27} - \dot{E}x_{HE-III}^Q = \dot{E}x_{d,HE-III}$
M−I	$\dot{m}_9 h_9 + \dot{m}_{41} h_{41} - \dot{m}_{42} h_{42} = 0$	$\dot{m}_9 ex_9 + \dot{m}_{41} ex_{41} - \dot{m}_{42} ex_{42} = \dot{E}x_{d,M-I}$
P1	$\dot{W}_{P1} = \frac{\dot{m}_9 \nu (P_9 - P_8)}{0.85}$	$\dot{m}_9 (ex_8 - ex_9) + \dot{W}_{P1} = \dot{E}x_{d,P1}$
HE-II	$\dot{Q}_{HE-II} = \left(\dot{m}_{44}(h_{44} - h_{45})\right)0.98 - \dot{m}_9(h_{10} - h_9)$	$\dot{m}_{44}(h_{44} - h_{45}) - \dot{m}_9(ex_{10} - ex_9) + \frac{\dot{Q}_{HE-II}}{T_0} = \dot{E}x_{d,HE-II}$
T/G	$\dot{W}_{T/G} = \dot{m}_{10}(h_{10} - h_{11})0.97$	$\dot{m}_{10}(ex_{10} - ex_{11}) - \dot{W}_{T/G} = \dot{E}x_{d,T/G}$
Con	$\dot{Q}_{Con} = \left(\dot{m}_{11}(h_{11} - h_8)\right)0.98 - \dot{m}_{24}(h_{25} - h_{24})$	$\dot{E}x_{d,Con} = \dot{m}_{11}(h_8 - h_{11}) - \dot{m}_{24}(ex_{25} - ex_{24}) + \frac{\dot{Q}_{Con}}{T_0}$
HTEL	$\dot{W}_{HTEL} + \dot{W}_{EH} + \dot{m}_8 h_8 - \dot{m}_9 h_9 - \dot{m}_{10} h_{10} = \dot{Q}_{HTEL}$	$\dot{W}_{HTEL} + \dot{W}_{EH} + \dot{m}_8 ex_8 - \dot{m}_9 ex_9 - \dot{m}_{10} ex_{10} - \dot{E}x_{HTEL}^Q = \dot{E}x_{d,HTEL}$
S	$\dot{m}_{10} h_{10} - \dot{m}_{11} h_{11} - \dot{m}_{12} h_{12} = 0$	$\dot{m}_{10} ex_{10} - \dot{m}_{11} ex_{11} - \dot{m}_{12} ex_{12} = \dot{E}x_{d,S}$
M−II	$\dot{m}_7 h_7 + \dot{m}_{11} h_{11} - \dot{m}_8 h_8 = 0$	$\dot{m}_7 ex_7 + \dot{m}_{11} ex_{11} - \dot{m}_8 ex_8 = \dot{E}x_{d,M-II}$
HE-IV	$\dot{Q}_{HE-IV} = \left(\dot{m}_{12}(h_{12} - h_{13})\right)0.98 - \dot{m}_{28}(h_{29} - h_{28})$	$\dot{m}_{12}(ex_{12} - ex_{13}) - \dot{m}_{28}(ex_{29} - ex_{28}) + \frac{\dot{Q}_{HE-IV}}{T_0} = \dot{E}x_{d,HE-IV}$
CB	$\dot{m}_{13} h_{13} - \dot{m}_{23} h_{23} - \dot{m}_{40} h_{40} - \dot{W}_C = \dot{Q}_{CB}$	$\dot{m}_{13} ex_{13} - \dot{m}_{23} hex_{23} - \dot{m}_{40} ex_{40} - \dot{W}_C - \frac{\dot{Q}_{CB}}{T_0} = \dot{E}x_{d,CB}$

Table 3
Combustion balance of ash-free lignite for the base case [39,43].

$\lambda = 1.68$ and $a = 0.02746$				
Reactant*		Product*		
C	0.0113810	CO_2	b	0.0108745
S	0.0001701	CO	c	0.0005065
N	0.0000120	SO_2	d	0.0001701
O	0.0012708	NO_2	e	0.0000120
H	0.0142992	N_2	f	0.1734737
Moisture (H_2O)	0.0174991	O_2	g	0.0289500
		$H_2O_{(gaseous)}$	h	0.0317983

*kmol/kg-lignite.

$$ex_i^{Ph} = c_p\left(T_i - T_0 - T_0 \bullet \ln\left(\frac{T_i}{T_0}\right)\right) \tag{8}$$

If the process includes a chemical reaction in itself, then the chemical term should be taken into account where is given by:

$$ex_{ch} = \sum_i x_i ex_{i,ch} + R_u T_0 \sum_i x_i \ln(x_i) \tag{9}$$

Here, h and s indicate respectively the enthalpy and entropy at a particular state. c_p is the specific heat of gas-phase flow. Subscript of 0 indicates the reference state conditions, taken as 25 °C and 1 atm in this study. P is the total pressure of the stream, x_i is the mole fraction, and $ex_{i,ch}$ standard chemical exergy of the i^{th} substance. The analysis was built on the four main structures, namely the boiler (B), *ORC* block (OB), *HTEL* block (HB), and compressor block (CB). The energy and exergy balances of the designed multi-purposed system are given in Table 2.

3.1. Boiler

The boiler, in which low-calorific lignite with high moisture and ash content is used, has a 150 MW capacity. The base (present) case was determined by the in-situ measurements where the unmeasured values were obtained from the mass balance of combustion reaction given by Eq (1). The detailed information about the measurement equipment and the used fuel can be seen in the authors' previous studies [42,43].

$$\overbrace{(C + H + N + S + O + H_2O_{(fluid)})}^{Reactant} + \lambda \cdot a \cdot \overbrace{(3.76 \cdot N_2 + O_2)}^{Air} + \overbrace{(O_2)}^{HTEL} \overbrace{\cdot b \cdot CO + c \cdot CO_2 + d \cdot NO_2 + e \cdot SO_2 + f \cdot O_2 + g \cdot N_2 + h \cdot H_2O_{(gaseous)}}^{Product} \tag{10}$$

Here, the term "a" indicates the coefficient of combustion air for the stoicheiometric condition, where λ indicates the coefficient of excess air. The elemental analysis of the lignite and the data of the combustion products for the base case are given in Table 3 [39,43].

The O_2 amount in the products is kept constant for the new system to get the same combustions conditions for the new system. By doing so, comparative situations are also formed. The new coefficient of excess is determined, taking the O_2 obtained from *HTEL* into consideration for the combustion process. In terms of reactants (R) and products (P), the heat obtained from the combustion reaction is given by the following equation [44]:

$$\dot{Q}_f = \sum_R \dot{n}\left(\overline{h}_0^f - \overline{h}_T - \overline{h}_{298}\right) - \sum_P \dot{n}\left(\overline{h}_o^f - \overline{h}_T - \overline{h}_{298}\right) \tag{11}$$

where, $\dot{Q}_f$ describes the heat of fuel. $\dot{n}$, $\overline{h}_0^f$, $\overline{h}_T$, and $\overline{h}_{298}$ are the mole ratio, molar enthalpy of formation, molar enthalpy at the temperature T, and molar enthalpy at 298 K, respectively. So, the exergy of the combustion process can be obtained by the following equation [45-47]:

Table 4
Thermophysical properties of cyclopentane [51,52].

	P_{cr} (kPa)	T_{cr} (°C)	Cp (kJ/kgK)	P (kg/m^3)	ODP*	GWP**
Cyclopentane	4520	238.5	708.9	1.96	0	7

* relative to R11, **relative to CO_2

Fig. 2. Structure of the handled HTEL cell.

$$\dot{E}x_f = \left(1 - \frac{T_0}{T_{cc}}\right)\dot{Q}_f - I \tag{12}$$

where T_{cc} indicates the temperature of the combustion chamber assumed as adiabatic combustion temperature, and I describes the exergy destruction rate and is given as in terms of generated entropy (S_g) and reference state temperature ($T_0 = 298$ K) [44]:

$$I = \dot{E}x_{d,f} = T_0 S_g \tag{13}$$

$$S_g = S_P - S_R \tag{14}$$

where S_R and S_P respectively define the entropies of reactants and products, which is calculated by the following equation [44]:

$$S_k = \sum_i \dot{n}_k\left(\overline{s}_k^o(T, P_0) - Rln(x_k P)\right); i = ProductorReactant \tag{15}$$

Here, $\overline{s}_i^o$, R, x_k, and P are orderly absolute molar entropy of the k^{th} component, the universal gas constant, mole ratio of the k^{th} compound, and total pressure of the flow. All the required data was obtained from the Ref [48].

3.2. ORC power block

The stack gases have still more available energy after it was used for the preheating of air in APH. Therefore, a supercritical ORC plant was designed to evaluate this waste heat. Since most of the refrigerant fluids have over-hanged saturated lines, the best choice would be to design the cycle over the critical points if the heat source is appropriate [49,50]. At the designing stage, the properties and kind of cooling fluid are the crucial issues. Air cooling is considered in this study to obtain combustion air with a higher temperature. The applicable temperature range of the working fluid, the critical temperature and pressure of the working fluid, and the environmental issues such as ozone depletion potential (ODP) and global warming potential (GWP) are also the other vital issues. In this study, cyclopentane was selected as the most appropriate working fluid depending on the authors' experiences [40]. The properties of cyclopentane are given in Table 4 [51,52].

In the analysis, the isentropic efficiencies for the pumps and turbine were assumed as 85%, whereas the generator efficiency was taken as 97%. The parasitic losses were taken as 2% of the initial conditions for both heat exchangers and pipes. The heat losses from the heat exchanger

surfaces were assumed as 2% of the heat energy of the source. The outlet temperature of stack gases was assumed as 130 °C considering the condensation of SO_2.

3.3. HTEL block

HTEL (solid oxide electrolyzer) is commonly used for H_2 production, depending on its higher efficiency. An HTEL decomposes water by using a solid oxide electrolyte to produce H_2 and O_2 [53]. The schematic of the handled HTEL cell structure is given in Fig. 2.

The reactions that occurred in the cathode, anode, and overall of an HTEL are respectively given as follows:

$$H_2O(g) + 2e^- \rightarrow H_2(g) + O^{2-} \tag{16}$$

$$O^{2-} \rightarrow \frac{1}{2}O_2(g) + 2e^- \tag{17}$$

$$H_2O(g) \rightarrow H_2(g) + \frac{1}{2}O_2(g) \tag{18}$$

Total energy required for the decomposition (ΔH) in a HTLE, includes electrical energy (ΔG; Gibbs free energy) and heat energy ($T\Delta S$) [53]:

$$\Delta H = \Delta G + T\Delta S \tag{19}$$

where S is the entropy. Neglecting kinetic and potential energy variation, as well as pressure drop and overpotentials due to crossover, the operating voltage of HTEL can be calculated as follows [54]:

$$V_{HTEL} = V_{rev} + (V_{act} + V_{con} + V_{ohm}) \tag{20}$$

where V_{act} and V_{con} are respectively the activation and concentration overpotentials for both cathode and anode. V_{ohm} is the ohmic overpotential for the cathode, anode, electrolyte, and interconnect layers. The reversible voltage (V_{rev}) of each cell is given by Nernst equation [55]:

$$V_{rev} = V_0 + \frac{RT}{2F} ln\left(\left(\frac{P^o_{H_2}\sqrt{P^o_{O_2}}}{P^o_{H_2O}\sqrt{P_{ref}}}\right)\right) \tag{21}$$

Here, R is the universal gas constant (=8.3145 J/molK), F is the Faraday constant (=9.6485·10^{4}C/mol). $P^o_{H_2}$, $P^o_{O_2}$, and $P^o_{H_2O}$ are respectively the partial inlet pressures, where P_{ref} is the reference pressure in Pa (=101325 Pa). V_0 is the standard potential and can be given by [56]:

$$V_0 = 1.253 - 2.4516\hat{A}\cdot 10^4 T \tag{22}$$

3.3.1. Activation overpotential

Activation overpotential ($V_{act,i}$) is defined by the activation polarization for cathode and anode sides. In terms of subscript i, which defines the cathode and anode, this polarization is calculated by Butler-Volmer equation [55]:

$$J = J_{0,i}\left[exp\left(\frac{\alpha nFV_{act,i}}{RT}\right) - exp\left(-\frac{(1-\alpha)nFV_{act,i}}{RT}\right)\right] \tag{23}$$

where J is the current density, α is the charge transfer coefficient and can be taken as 0.5 for water electrolysis [57], and n is the number of transferred electrons (=2). J_0 defines the exchange current density and is given by [54]:

$$J_{0,i} = \gamma_i exp\left(-\frac{E_{act,i}}{RT}\right) \tag{24}$$

where γ_i and $E_{act,i}$ are respectively the pre-exponential coefficients, and activation energy for cathode and anode sides. Finally, the activation overpotential is given as [54]:

$$V_{act,l} = \frac{RT}{F} sinh^{-1}\left(\frac{J}{2J_{0,l}}\right) \tag{25}$$

3.3.2. Concentration overpotential

Concentration overpotential is occurred with the diffusive transportation of steam-H_2 binary mixture and O_2 to/from the reaction domain at the cathode and anode sides. Fick's model can be used to calculate the concentration overpotentials [58]. It is given for cathode ($V_{con,c}$) and anode ($V_{con,a}$) as:

$$V_{con,c} = \frac{RT}{2F} ln\left[\left(\frac{1 - \frac{JRT\delta_c}{2FD^{eff}_{H_2O}P^I_{H_2}}}{1 + \frac{JRT\delta_c}{2FD^{eff}_{H_2O}P^I_{H_2O}}}\right)\right] \tag{26}$$

$$V_{con,a} = \frac{RT}{2F} ln\left[\left(1 + \frac{JRT\delta_a}{4FD^{eff}_{O_2}P^I_{O_2}}\right)^{\frac{1}{2}}\right] \tag{27}$$

where F, δ_c and δ_a are respectively Faraday constant (=96485C/mol) the thickness of the cathode and anode layer. $P^I_{H_2}$, $P^I_{H_2O}$ and $P^I_{O_2}$ are respectively the partial pressures of H_2, steam, and O_2 at the electrode surfaces. $D^{eff}_{O_2}$ and $D^{eff}_{H_2O}$ are respectively the effective diffusion coefficient of O_2 and H_2O. $D^{eff}_{O_2}$ is given by [58]:

$$\frac{1}{D^{eff}_{O_2}} = \frac{\zeta}{\varepsilon}\left(\frac{1}{D_{O_2,M}} + \frac{1}{D_{O_2,k}}\right) \tag{28}$$

where ζ, ε, $D_{O_2,M}$ and $D_{O_2,k}$ are respectively porosity, tortuosity, molecular and Knudsen diffusions of anode side. $D_{O_2,k}$ can be given by the kinetic theory [59]:

$$D_{O_2,k} = \frac{4}{3} r\sqrt{\frac{8RT}{\pi M_{O_2}}} \tag{29}$$

where r is pore radius and M_{O_2} is the molecular weight of steam (=31.999 kg/kmol). Assuming O_2 is an ideal gas, $D_{O_2,M}$ can be given by [55]:

$$D_{O_2,M} = 0.0026\frac{T^{\frac{3}{2}}}{(M_{O_2})^{\frac{1}{2}}P_{ref}\sigma^2_{O_2}\Omega_{D,O_2}} \tag{30}$$

where σ_{O_2} is the collision diameter of O_2 and is given as 3.467 [55]. Ω_{D,O_2} is the diffusion collision integral. It can be calculated by the following formulation [55]:

$$\Omega_{D,O_2} = \frac{1.06036}{(T^*)^{0.1561}} + \frac{0.193}{\exp(0.47635T^*)} + \frac{1.03587}{\exp(1.52996T^*)} + \frac{1.76474}{\exp(3.89411T^*)} \tag{31}$$

where T^* is given by:

$$T^* = \frac{\kappa T}{\varepsilon_{O_2}} \tag{32}$$

where κ (1.38066·10^{-23} J/K) is the Boltzmann's constant. ε_{O_2} is the Lennard–Jones length, and is given as [55]:

$$\frac{\varepsilon_{O_2}}{\kappa} = 106.7 \tag{33}$$

The cathode side can be calculated in a similar way as given by following:

$$\frac{1}{D^{eff}_{H_2O}} = \frac{\zeta}{\varepsilon}\left(\frac{1}{D_{H_2O-H_2}} + \frac{1}{D_{H_2O,k}}\right) \tag{34}$$

where $D_{H_2O-H_2}$ and $D_{H_2O,k}$ are respectively molecular and Knudsen diffusions of cathode side. Knudsen diffusion is given by:

$$D_{H_2O,k} = \frac{4}{3} r\sqrt{\frac{8RT}{\pi M_{H_2O}}} \tag{35}$$

where M_{H_2O} is the molecular weight of steam (=18.015 kg/kmol).

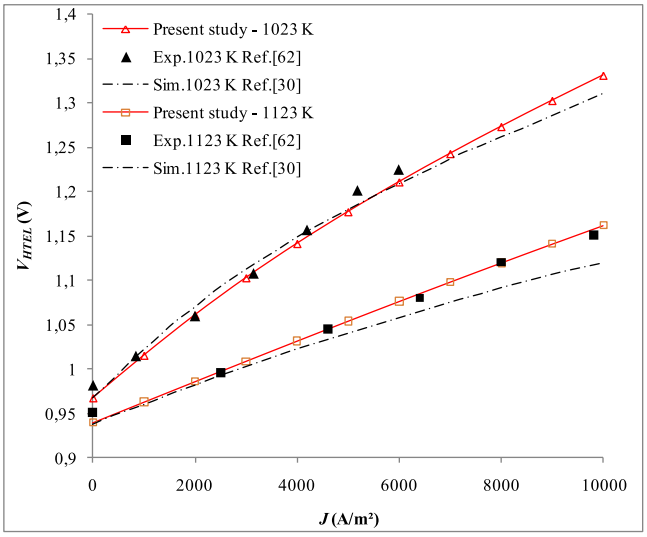

Fig. 3. Validation of the model.

Molecular binary diffusion can be given by Chapman-Enskog theory [59]:

$$D_{H_2O-H_2} = 0.00133\left(\frac{1}{M_{H_2O}}+\frac{1}{M_{H_2}}\right)^{\frac{1}{2}}\frac{T^{\frac{3}{2}}}{P_{ref}\sigma^2_{H_2O-H_2}\Omega_{D,H_2O-H_2}} \quad (36)$$

where M_{H_2} is the molecular weight of hydrogen (=2.016 kg/kmol)., T is the working temperature of HTEL, P_{ref} is the reference pressure in atm (=1 atm). $\sigma_{H_2O-H_2}$ is collusion diameter of the binary mixture and is given as the average collision diameter of H_2 (σ_{H_2} = 2.827) and steam (σ_{H_2O} = 2.641) [59]:

$$\sigma_{H_2O-H_2} = \frac{\sigma_{H_2}+\sigma_{H_2O}}{2} \quad (37)$$

Ω_{D,H_2O-H_2} is the diffusion collision integral of the binary mixture and can be calculated by Eq (31). However, the term T^* is given by:

$$T^* = \frac{\kappa T}{\varepsilon_{H_2O-H_2}} \quad (38)$$

where $\varepsilon_{H_2O-H_2}$ is the Lennard–Jones length of the binary mixture, and is calculated in terms of the Lennard–Jones lengths of steam (ε_{H_2O} = κ•809.1) and H_2 (ε_{H_2} = κ•59.7) as following [55]:

$$\frac{\varepsilon_{H_2O-H_2}}{\kappa} = \sqrt{\frac{\varepsilon_{H_2O}}{\kappa}\frac{\varepsilon_{H_2}}{\kappa}} \quad (39)$$

3.3.3. Ohmic overpotential

The ohmic overpotential occurs due to electrical and ionic resistances at electrode, electrolyte, and interconnect layers. It is given as:

$$V_{ohm} = \left(\frac{\delta_c}{\tau_c}+\frac{\delta_e}{\tau_e}+\frac{\delta_a}{\tau_a}+2\frac{\delta_i}{\tau_i}\right)J \quad (40)$$

where δ_c, δ_e, δ_a and δ_i are respectively the thicknesses of cathode, electrolyte, anode, and interconnects. τ_c, τ_e, τ_a and τ_i represent the electrical conductivities for cathode, electrolyte, anode, and interconnects, respectively. The electrical conductivities can be calculated in terms of temperature (T) by the following equations [60]:

$$\tau_c = \frac{4.2\bullet10^7}{T}\,exp\left(\frac{-1200}{T}\right) \quad (41)$$

$$\tau_e = 3.34\bullet10^4\exp\left(\frac{-10300}{T}\right) \quad (42)$$

$$\tau_a = \frac{9.5\bullet10^7}{T}\,exp\left(\frac{-1150}{T}\right) \quad (43)$$

Table 5
The results of statistical evaluation of the model.

	T_{HTEL} = 1023 K			T_{HTEL} = 1123 K		
	R^2	*CoV*	*RMSE*	R^2	*CoV*	*RMSE*
Ref [25]	0.9940	0.7228	0.0599	0.9973	0.5029	0.0752
Ref [51]	0.9996	1.2366	0.0458	0.9976	0.4591	0.0715

Table 6
The properties of the HTEL block.

Property	Unit	Value	Reference
Anode thickness, δ_a	m	$17.5\cdot10^{-6}$	[61]
Cathode thickness, δ_c	m	$312.5\cdot10^{-6}$	[61]
Electrolyte thickness, δ_e	m	$12.5\cdot10^{-6}$	[61]
Pore diameter, r	μm	1.07	[54]
Porosity, ζ	–	0.3	[65]
Tortuosity, ε	–	5.0	[65]
Cell area	m^2	0.010	[25]
Cell active area, A_{cell}	m^2	0.008	[25]

$$\tau_i = \frac{9.3\bullet10^5}{T}\,exp\left(\frac{-1100}{T}\right) \quad (44)$$

3.3.4. Validation

The obtained model is compared and validated with the data in the literature. The same parameters in Ref [29] and Ref [61] are used for this aim. The data presented by Ref [29] and [61] was obtained by the matching method. The data given in the related studies was degraded using Excel software. So, the obtained curves and given data are matched by one-to-one correspondence. Later, the present model results added the figure and compared statistically with the related literature data. The validation of the model is given in Fig. 3.

The obtained results are evaluated by some statistical parameters such as R^2 (percentage of absolute change), CoV (coefficient of variation), and RMSE (root mean square error) [62-64]. The statistical results are given in Table 5.

According to Table 4, the model is agreeable with both Ref [29] and Ref [61]. The handled model is more suitable than the simulation values of Ref [29] and the experimental values of Ref [61]. At the higher current density values, the difference between the present and Ref [25] increases depending on the ohmic overpotential of interconnect layers.

3.3.5. Evaluation of overall HTEL block

The required electricity for the HTEL block is obtained from the ORC block. For a single cell, the electricity need is calculated by:

$$\dot{W}_{elec} = JV_{HTEL}A_{cell} \quad (45)$$

where A_{cell} is the active area of the HTEL cell. The properties of the HTEL block are given in Table 6.

The required cell number is calculated by:

$$N_{cell} = \frac{\dot{W}_{HTEL}}{\dot{W}_{elec}} = \frac{\dot{W}_{T/G}-\dot{W}_{P1}}{\dot{W}_{elec}} \quad (46)$$

Finally, the energy and exergy balance equations of the HB are as follows:

$$\dot{Q}_{HB} = \dot{m}_7h_7 - \dot{m}_{12}LHV - \dot{W}_{HTEL} - \dot{W}_{EH} \quad (47)$$

$$\dot{E}x_{d,HB} = \dot{m}_7ex_7 - \dot{E}x_{HTEL} - \dot{W}_{HTEL} - \dot{W}_{EH} - \frac{\dot{Q}_{HB}}{T_0} \quad (48)$$

where LHV is the higher heating value of H_2 (=240,000 kJ/kmol). $\dot{E}x_{HTEL}$ is the exergy output of the HTEL block, and it can be defined as maximum electricity generation ability when the HTEL is worked as a fuel cell. So, it can be given as:

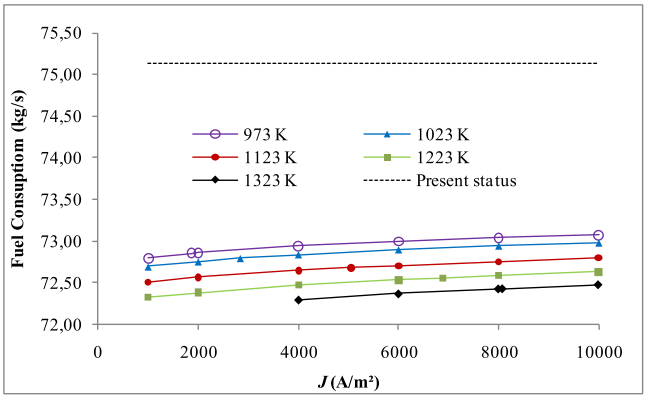

Fig. 4. Variation of fuel consumption.

$$\dot{E}x_{HB} = V_o J A_{\text{cell}} N_{\text{cell}} \tag{49}$$

The energy and exergy efficiencies can respectively be given by:

$$\eta_{HB} = \frac{\dot{m}_{H_2} LHV}{\dot{W}_{HTEL} + \dot{W}_{EH} + \dot{E}_7} \tag{50}$$

$$\varepsilon_{HTEL} = \frac{\dot{E}x_{HTEL}}{\dot{W}_{HTEL} + \dot{W}_{EH} + \dot{E}x_7} \tag{51}$$

3.4. Compressor block

The required power for compressor block ($\dot{W}_{CB}$) is calculated by [44]:

$$\dot{W}_C = \dot{m} C_P \frac{T_{19}}{\eta_C} \left[\left(\frac{P_o}{P_i} \right)^{\frac{k-1}{k}} - 1 \right] n \tag{52}$$

where C_P is the specific heat (=14.4 kJ/kgK), η_C is the compressor efficiency (=70%), and k is the isentropic exponent (=1.4). n indicates the number of compression stages (taken as 5 in this study). The compression ratio was calculated as 3.72, giving the minimum compressor power requirement.

4. Results and discussions

The designed system aims to produce H_2 as a valuable fuel, improve boiler efficiency using the produced O_2 for the enrichment of the combustion air, and generate domestic hot water for internal heating purposes. The designed system was then evaluated using the energy and

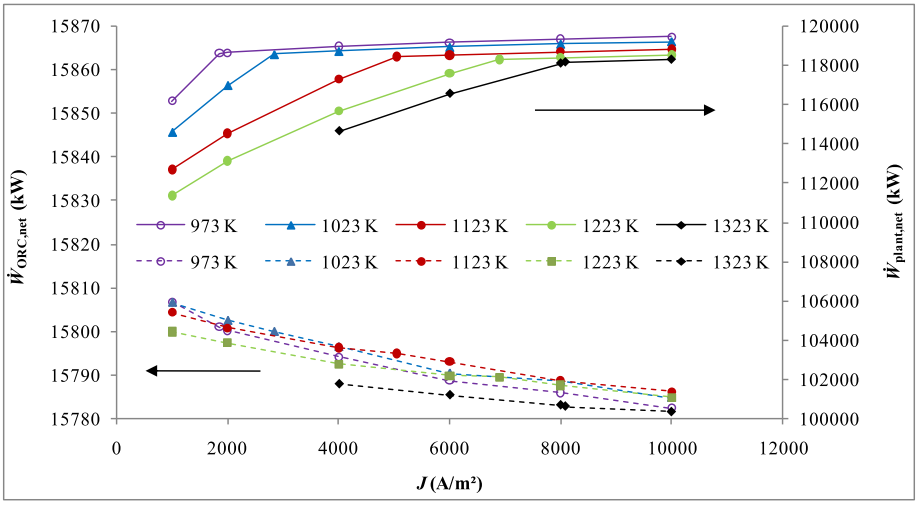

Fig. 5. Net Power outputs of the ORC and whole plant.

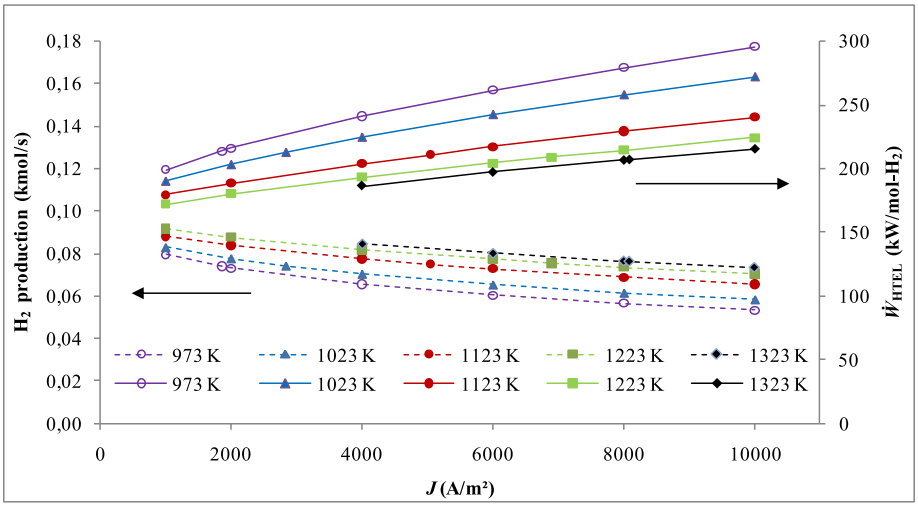

Fig. 6. Variation of H_2 production and the required electricity.

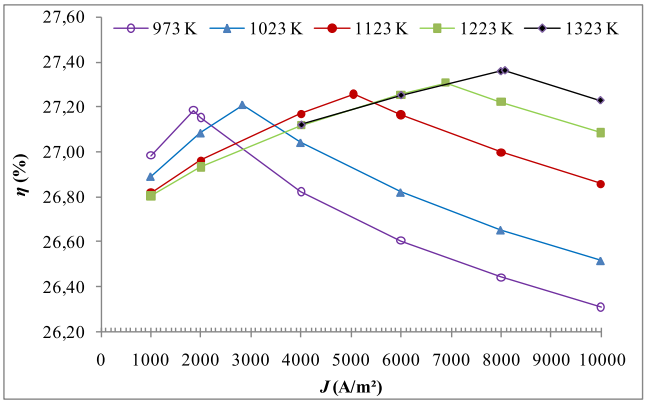

Fig. 7. Energy efficiency variation of the new design.

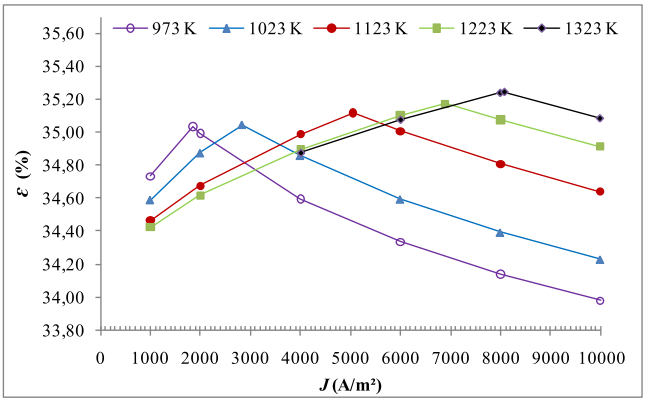

Fig. 8. Exergy efficiency variation of the new design.

exergy analysis method for different parameters such as HTEL working temperature and current density values to conduct the best choice.

In the study, the present characteristics of working conditions of the boiler were tried to be kept constant. By doing so, it was aimed to prevent the fundamental changes, which ultimately would affect the whole plant from the economic and design points of view, in the other parts of the plants (such as turbine, condenser, and heat exchangers) for the steam side. In this regard, fuel consumption is the variable working characteristic. The fuel consumption variation is given in Fig. 4.

According to Fig. 4, the fuel consumption increase with the increase of current density and decrease of HTEL temperature. This is why the increase in the current density causes an increase in the required power of HTEL. Since the required power is generated from the waste heat of stack gases and the main characteristics of the power plant (such as temperature and pressure values) are preserved, a decrease in O_2 production occurs depending on this increase in the power consumption of HTEL. So, the combustion efficiency decrease and fuel consumption increase. The variation was recorded as ranging between 72.29 kg/s and 73.07 kg/s. This variation shows that it is available to save fuel in a range of 2.74 to 3.78% compared to the present consumption (=75.13 kg/s). Related to this consumption, the net power generations of the *ORC* and the whole plant are given in Fig. 5.

According to Fig. 5, the power generation ability of ORC (dashed line) ranges between 15,781.51 kW and 15,806.76 kW. The generation ability rate decrease with the increase of the current density. After 8,000 A/m^2, the net power generations are very close to each other for the handled temperatures. The net power generation values are relatively higher for the lower current densities at the lower HTEL temperature. This situation arises from the higher fuel consumption resulting in higher stack gases volume and temperature. The whole plant power generation (continuous line) decreases in contrast to the ORC. It changes between 111,376.53 and 119,467.95 kW, where it is 124,777.26 kW for the present status of the plant. The decrease rate for the 1023 K is higher than the higher HTEL temperatures. The leading cause of this decrease is the used heat energy in the combustion chamber for obtaining the required heat of HTEL that directly affects the transferred energy to the steam of the whole plant. For the net power generation of the plant, there are breaking points at lower current densities, which change with the increase of working temperatures. At higher temperatures, the breaking points occur at higher current densities. After these breaking points, the net power generation slightly changes since the internal heat generation of HTEL is enough to split the water. The change of H_2 production rate and required electricity per unit H_2 production is shown in Fig. 6.

According to Fig. 6, H2 production (dashed line) decreases with the increase of current density and increases with the increase of HTEL temperature. According to Faraday's law, H_2 and O_2 production should increase. However, depending on the structural analysis in which the

Table 7
The technical characteristics of the HTEL block.

Property	Unit	Value	Reference
Cell operating pressure	kPa	101.325	–
Cell operating temperature	K	1123	–
Current density, J	A/m^2	5052	–
H_2O molar fraction	%	90	[60]
O_2 molar fraction	%	100	[60]
Steam utilization factor	%	60	[65]
Calculated effective diffusion coefficient at the anode, $D^{eff}_{O_2}$	–	$3.0202 \cdot 10^{-6}$	–
Calculated effective diffusion coefficient at the cathode, $D^{eff}_{H_2O}$	–	$2.8002 \cdot 10^{-6}$	–
Anode activation energy, $E_{act,a}$	J/mol	120,000	[54]
Cathode activation energy, $E_{act,c}$	J/mol	100,000	[54]
Coefficients for exchange current density for the anode, γ_a	A/m^2	$2.051 \cdot 10^9$	[54]
Coefficients for exchange current density for the cathode, γ_c	A/m^2	$1.344 \cdot 10^{10}$	[54]
H_2 production rate	kmol/s	0.0748	–
O_2 production rate	kmol/s	0.0374	–
Required heat, $T\Delta S$	kJ/mol-H_2	37.6	–
Required electricity, W_{HTEL} (ΔG)	kJ/mol-H_2	211.0	–
Required energy, ΔH	kJ/mol-H_2	248.6	–
Cell number	–	1645	–

present status and characteristics of the power plant are preserved, the power requirement increase with the increase of current density. So, the H_2 and O_2 production decrease in the viewpoint of the generated power from the waste heat of stack gases. The produced H_2 changes between 0.0534 and 0.0918 kmol/s. According to these results, the produced O_2 directly affects the boiler's combustion phenomena and changes in the same trend. The required electricity (continuous line) increases with the decrease of HTEL temperature and increases with the current density as appropriate to literature records. This requirement changes between 172.1 and 295.7 kW/mol-H_2. In light of these results, the new design's calculated energy and exergy efficiencies are given in Figs. 7 and 8.

According to Figs. 7 and 8, the energy and exergy efficiencies increase up to a certain point with the increase of the current density for all HTEL temperatures, and then it starts to decrease. These values increase with the increase of HTEL temperature.

In this regard, peak points called optimum points occurs in the designs. Even though the net power generation increases sharply until these peak points (see Fig. 5) depending on the decrease of the internal heat demand of HTEL, the required power of HTEL also increases. This situation negatively affects the production of H2 (the harvesting material with high energy quality). This is the leading cause of the increase in

Table 8
The functional properties of the designed system.

Nokta	Fluid	T (K)	P (kPa)	n (kmol/s) m* (kg/s)	h (kJ/kmol) h* (kJ/kg)	s (kJ/kmolK) s* (kJ/kgK)	ex^{Ph} (kW)	ex^{Ch} (kW)
0	H_2O	298.15	101.325	–	1,885.86	6.72	–	–
	O_2				8,672.32	205.03		
	H_2				7,863.60	130.62		
	Air				8,662.19	194.38		
	Cyclopentane*				−45.23	−0.15		
1	H_2O*	493.15	15,730.9	131.11311	943.55	2.52	197.64	–
2	H_2O*	622.15	3,432.0	119.78112	3,103.91	6.67	1,120.57	–
3	H_2O*	811.15	13,729.0	131.11311	3,430.98	6.54	1,486.45	–
4	H_2O*	811.15	3,383.0	119.78112	3,539.18	7.28	1,372.59	–
5a	H_2O	298.15	101.325	0.33881	1,885.86	6.72	46,336,0	–
5b	H_2O	298.33	107.70	0.33881	1.,895.66	6.75	46,440.9	–
6a	H_2O	309.12	105.55	0.00103	2,711.09	9.32	48.25	–
6b	H_2O	309.12	105.55	0.33778	2,711.09	9.32	48.25	–
7	H_2O	1,123.00	101.33	0.00103	77,067.16	237.48	6,380.90	9,500.00
8	H_2O	1,123.00	101.33	0.00172	77,067.16	237.48	6,380.90	9,500.00
9	H_2	1,123.00	101.33	0.00019	32,288.66	169.61	12,800.79	236,100.00
	O_2	1,123.00	101.33	0.00052	35,694.53	247.54	14,346.63	3,970.00
10	H_2O	1,123.00	101.33	0.00069	77,067.16	170.26	26,421.13	6,967.51
11	H_2	1,123.00	101.33	0.00122	32,288.66	169.61	12,800.79	234,993.74
	H_2O	1,123.00	101.33	0.00069	77,067.16	170.26	26,421.13	8,892.39
12	H_2	1,123.00	101.33	0.00019	32,288.66	169.61	12,800.79	232,317.18
	H_2	1,123.00	101.33	0.00103	32,288.66	169.61	12,800.79	236,100.00
13	H_2	349.12	98.29	0.00103	9,337.94	135.13	130.80	236,100.00
14	H_2	509.84	365.62	0.00103	14,033.04	146.19	1,538.64	236,100.00
15	H_2	349.12	365.62	0.00103	9,337.94	135.13	141.72	236,100.00
16	H_2	509.84	1,360.11	0.00103	14,033.04	146.19	1,549.56	236,100.00
17	H_2	349.12	1,360.11	0.00103	9,337.94	135.13	152.64	236,100.00
18	H_2	509.84	5,059.61	0.00103	14,033.04	146.19	1,560.49	236,100.00
19	H_2	349.12	5,059.61	0.00103	9,337.94	135.13	163.57	236,100.00
20	H_2	509.84	18,821.75	0.00103	14,033.04	146.19	1,571.41	236,100.00
21	H_2	349.12	18,821.75	0.00103	9,337.94	135.13	174.49	236,100.00
22	H_2	509.84	70,016.93	0.00103	14,033.04	146.19	1,582.33	236,100.00
23	H_2	349.12	70,016.93	0.00103	9,337.94	135.13	185.41	236,100.00
24	Air	298.15	109.84	1.10730	8,662.19	194.38	200.07	128.49
25	Air	329.12	107.65	1.10730	9,566.56	197.23	203.98	128.49
26	Air	329.12	106.57	0.89014	9,566.56	133.44	19,199.79	128.49
27	Air	318.15	104.44	0.89014	9,246.04	132.47	19,117.62	128.49
28	Air	329.12	106.57	0.21716	9,566.56	197.23	179.07	128.49
29	Air	332.77	104.44	0.21716	9,673.30	197.55	140.78	128.49
30	Air	332.77	104.44	0.04343	9,673.30	197.55	140.78	128.49
31	Air	336.12	102.35	0.04343	9,771.15	197.84	102.41	128.49
32	Air	332.77	104.44	0.04343	9,673.30	197.55	140.78	128.49
33	Air	336.12	102.35	0.04343	9,771.15	197.84	102.41	128.49
34	Air	332.77	104.44	0.04343	9,673.30	197.55	140.78	128.49
35	Air	336.12	102.35	0.04343	9,771.15	197.84	102.41	128.49
36	Air	332.77	104.44	0.04343	9,673.30	197.55	140.78	128.49
37	Air	336.12	102.35	0.04343	9,771.15	197.84	102.41	128.49
38	Air	332.77	104.44	0.04343	9,673.30	197.55	140.78	128.49
39	Air	336.12	102.35	0.04343	9,771.15	197.84	102.41	128.49
40	Air	336.12	102.35	0.21716	9,771.15	197.84	102.41	128.49
41	Air	541.70	101.33	0.21716	15,861.72	211.98	1,953.03	128.49
42	Enriched air	541.70	101.33	0.21768	15,910.87	212.10	1,967.27	128.46
43	Flue gas	747.28	101.33	–	−8,629.81	54.22	–	–
44	Flue gas	576.48	101.33	–	−9,982.65	52.18	–	–
45	Flue gas	403.15	101.33	–	−11,298.23	49.44	–	–
46*	Cyclopentane	322.35	101.33	0.03202	0.00	0.00	1.75	–
47*	Cyclopentane	324.53	4,739.58	0.03202	533.07	0.25	461.30	–
48*	Cyclopentane	513.15	4,550.00	0.03202	40,799.00	93.38	12,959.51	–
49*	Cyclopentane	368.11	105.55	0.03202	31,918.20	98.04	2,690.22	–

* values in mass rate (kg/s).

energy and exergy efficiencies. Besides, the O_2 production also decreases, which negatively affects the combustion process. This does not only means more fuel requirement but also means less power generation from ORC depending on the quality of stack gases.

The highest energy efficiencies of the designed system are obtained as 27.19%, 27.21%, 27.26%, 27.31%, and 27.36% for the HTEL temperature of 973 K, 1023 K, 1123 K, 1223 K, and 1323 K, respectively. The highest exergy efficiencies of the designed system are obtained as 35.03%, 35.05%, 35.12%, 35.17%, and 35.25% for the HTEL temperature of 973 K, 1023 K, 1123 K, 1223 K, and 1323 K, respectively. The highest energy and exergy efficiencies are obtained at the current densities of 1855, 2837, 5052, 6895, and 8084 A/m^2 for the HTEL temperature of 973 K, 1023 K, 1123 K, 1223 K, and 1323 K, respectively.

It is available to increase the energy efficiency between 15.78% and 16.53% compared to the plant's present energy efficiency, which is equal to 23.48% [22]. For the exergy efficiency, this range is recorded between 20.43% and 21.16% compared to the plant's present exergy efficiency, which is equal to 29.09% [22]. The operating temperature is

Table 9
The analysis results of the designed system.

Component	E_i (kW)	E_o (kW)	Q (kW)	W (kW)	Ex_i (kW)	Ex_o (kW)	Ex_d (kW)	η (%)	ε (%)
B	1,067,906.53	879543.23	−188,363.30	–	597,191.79	359,303.55	238,520.02	82.36	60.06
APH	98,318.64	96,123.66	−2,194.98	–	5,4030.15	29,207.11	24,830.41	97.77	54.06
HE-I	202.96	5,769.37	5,566.42	–	4,321.21	1,188.87	3,132.34	100.00	27.51
T/G	94,939.31	74,273.68	−3,626.82	17,038.81	30,156.78	6,260.15	6,869.99	82.45	77.22
Con	74,273.68	72,777.86	−1,495.82	−1,207.70	10,161.19	3,627.82	6,538.37	96.42	35.65
HE-II	95,611.08	93,698.86	−1,912.22	–	37,441.97	26,999.21	10,449.17	98.00	72.09
P1	23.10	1,080.43	−186.59	−1,243.92	23.10	1,080.43	187.21	85.00	84.95
HE-III	20,734.58	20,319.89	−414.88	−0.19	1,642.32	367.00	1,276.89	98.00	22.26
HE-IV	1,718.13	1684.65	−33.48	–	1,022.53	166.93	855.71	98.00	16.31
HB	5,769.37	17,966.79	−3,597.86	−15,795.29	1,188.87	13,711.35	3,284.87	83.32	80.73
CB	153,366.67	154,911.08	−2,826.81	−4,371.21	21,934.36	21,332.96	4,982.10	98.21	81.06
Overall system	514,046.77	21,664.18	−199,086.34	118,453.37	387,733.53	17,714.74	300,927.09	27.26	35.12

selected as 1123 K taking the most available conditions of the literature into account. According to this selection, the technical details of the HTEL block are given in Table 7.

The working conditions of the designed plant were determined using the parameters given in Table 6. These parameters are given in Table 8. According to these operating parameters, detailed energy and exergy analysis were conducted. The results of the analysis of the designed plant are given in Table 9.

According to Table 9, the energy and exergy efficiencies of the overall system were respectively determined as 27.26 % and 35.12%. These results mean an increase of 16.09% in energy efficiency and an increase of 20.73% in exergy efficiency compared to the present status of the plant. The energy efficiencies of the boiler, ORC block, and HTEL block were respectively calculated as 82.36%, 16.52%, and 83.32%. The exergy efficiencies of the boiler, ORC block, and HTEL block were respectively calculated as 60.06%, 16.55%, and 74.18%. The consumed fuel was determined as 72.68 kg/s with a decrease of 3.27% compared to the present status. This reduction also means a decrease in the emissions in the same amount. In this case, the annual produced H_2 was determined as 479.14 kmol considering an operating time of 6400 h per year. The net electricity output of the plant was 118,453.37 kW, whereas the domestic hot water production was 3,697.40 kW.

According to the analysis results, the optimal current densities were determined as 1855, 2837, 5052, 6895, and 8084 A/m^2 for the HTEL temperature of 973, 1023, 1123, 1223, and 1323 K, respectively. Taking a yearly working time of 6400 h for the plant, the produced H_2 was calculated as 473.16, 475.27, 479.14, 483.15, and 487.79 kmol for the HTEL temperature of 973, 1023, 1123, 1223, and 1323 K, respectively. The HTEL energy-exergy efficiencies were calculated as 84.35–78.69%, 84.03–77.13%, 83.32–74.18%, 82.60–71.21% and 81.92–68.09% for the HTEL temperature of 973, 1023, 1123, 1223 and 1323 K, respectively. The supplied net power from the ORC block for the electrolyzer ranges between 15,781.51 and 15,806.76 kW with an energy efficiency of 16.52% and an exergy efficiency of 16.55%. The utilization of the waste heat of stack gases for power generation and the utilization of this power for H_2 production is the main factor that improves the energy and exergy efficiency of the plant. The utilization of the other product of O_2 in the combustion air improves the boiler efficiency since it increases the efficiency of the combustion process. This also decreases the fuel consumption for the same outputs, increasing energy and exergy efficiency. The waste heat recovery from the H2 storage system for the pre-heating of combustion air also improves the combustion process, increasing energy and exergy efficiency. The boiler energy efficiency were determined as 80.29%, 82.32%, 82.36%, 82.41% and 82.46% for the HTEL temperature of 973, 1023, 1123, 1223 and 1323 K, respectively. The exergy efficiencies were 60.07%, 60.06%, 60.06%, 60.05% and 60.05% in order. It means an increase of about 2% in the energy exergy efficiencies compared to present status with an energy efficiency of 80.68% and exergy efficiency of 58.91%. Finally, the recovery of the waste heat from ORC block for the pre-heating of electrolyzer water and domestic hot water also increases the energy and exergy efficiency with less impact than the issues mentioned above. The domestic water energy was calculated as 3,696.98, 3697.39, 3697.40, 3,697.34 and 3,696.96 kW for the HTEL temperature of 973, 1023, 1123, 1223 and 1323 K, respectively. The net power generation was determined as 118,640.39, 118,572.12, 118,453.37, 118.322.99, 118,183.62 kW for the HTEL temperature of 973, 1023, 1123, 1223 and 1323 K, respectively.

5. Conclusions

A multi-generation system including power generation, domestic hot water, and H_2 production was designed for the waste recovery of a 150 MW coal-fired power plant. In this regard, a high temperature electrolyzer sourced by a supercritical ORC cycle was added to existing system. Besides, the other product of O_2 was evaluated for the improvement of combustion. The waste of the stack gases fed the ORC unit. The present working conditions of the existing boiler were saved in the study. A high-temperature electrolyzer was integrated into the present system to produce H_2. The second product of O_2 from the electrolyzer was used to enrich the combustion process. The required power for the electrolyzer was obtained from a bottoming ORC cycle. The study shows that it is available to produce H_2 as the energy harvesting material in an amount ranging between 473.16 and 487.79 kmol with an energy efficiency of up to 84.35% and exergy efficiency up to 78.69%. It also shows that it is available to increase the boiler's energy and exergy efficiencies by about 2% compared to present status with an energy efficiency of 80.68% and exergy efficiency of 58.91%. It is available to obtain domestic hot water with an energy value of up to 3,696.98 kW. Despite the decrease in the power generation of about 4.92–5.28%, it is available to increase the overall energy efficiency of the whole plant up to 27.36% and exergy efficiency up to 35.25%.

The electrolyzer unit is a handy tool to improve the existing old-fashion power plants since it produces H_2 as the energy harvesting material and O_2 as the improver of the combustion process. However, the HTELs need more heat energy for their own internal needs. According to the knowledge of the authors, PEMEL is an alternative. In this regard, a standard PEMEL has a more negligible effect than HTEL's. So, the authors offer PEMELs working under a relatively higher temperature than standard PEMELs or solid oxide electrolyzers working under a relatively lower temperature than HTELs.

CRediT authorship contribution statement

Oguz Arslan: Conceptualization, Methodology, Validation, Investigation, Supervision, Writing – review & editing. **Emin Acikkalp:** Data curation, Investigation, Resources. **Gamze Genc:** Data curation, Investigation, Resources.

Declaration of Competing Interest

The authors declare that they have no known competing financial interests or personal relationships that could have appeared to influence the work reported in this paper.

References

[1] Song W, Quyang Z, Wang M, Li S, Liu J, Yu Q, et al. The combustion and NOx emission characteristics of the ultra-low volatile fuel using the novel pulverized coal self-sustained preheating combustion technology. Fuel 2020;271:117592.
[2] Chen H, Wu Y, Qi Z, Chen Q, Xu G, Yang Y. Improved combustion air preheating design using multiple heat sources incorporating bypass flue in large-scale coal-fired power nit. Energy 2019;169:527–41.
[3] Chen H, Qi Z, Dai L, Li B, Hu G, Yang Y. Performance evaluation of a new conceptual combustion air preheating system in a 1000 MW coal-fueled power plant. Energy 2020;193:16739.
[4] Liu M, Yan J, Wang J, Chong D, Liu J. Thermodynamic Analysis on a Pre-Dried Lignite-Fired Power System: Comparison on Energy Supply Systems for Dryer. Energy Procedia 2014;61:1924–7.
[5] Liu M, Jan J, Bai B, Chong D, Guo X, Xiao F. Theoretical Study and Case Analysis for a Predried Lignite-Fired Power System. Drying Technol 2011;29:1219–29.
[6] Xu C, Xu G, Zhao S, Zhou L, Yang Y, Zhang D. An improved configuration of lignite pre-drying using a supplementary steam cycle in a lignite fired supercritical power plant. Appl Energy 2015;160:882–91.
[7] Rao Z, Zhao Y, Huang C, Duan C, He J. Recent developments in drying and dewatering for low rank coals. Prog Energy Combust Sci 2015;46:1–11.
[8] Han X, Liu M, Zhai M, Chong D, Yan J, Xiao F. Investigation on the off-design performances of flue gas pre-dried lignite-fired power system integrated with waste heat recovery at variable external working conditions. Energy 2015;90:1743–58.
[9] Arslan O, Erbas O. Investigation on the improvement of the combustion process through hybrid dewatering and air pre-heating process: A case study for a 150 MW coal-fired boiler. J Taiwan Inst Chem Eng 2021;121:229–40.
[10] Yin C, Yan J. Oxy-fuel combustion of pulverized fuels: Combustion fundamentals and modeling. Appl Energy 2016;162:742–62.
[11] Tiwari HP, Das A, Singh U. Novel technique for assessing the burnout potential of pulverized coals/coal blends for blast furnace injection. Appl Therm Eng 2018;130:1279–89.
[12] Zhou A, Xu H, Tu Y, Zhao F, Zheng Z, Yang W. Numerical investigation of the effect of air supply and oxygen enrichment on the biomass combustion in the grate boiler. Appl Therm Eng 2019;156:550–61.
[13] Bamisile O, Huang Q, Dagbasi M, Kemena AD. Performance analysis of a novel solar PTC integrated system for multi-generation with hydrogen production. Int J Hydrogen Energy 2020;45:190–206.
[14] Safari F, Dincer I. Assessment and optimization of an integrated wind power system for hydrogen and methane production. Energy Convers Manage 2018;177:693–703.
[15] Balta MT, Dincer I, Hepbasli A. Thermodynamic assessment of geothermal energy use in hydrogen production. Int J Hydrogen Energy 2009;34:2925–39.
[16] Gokcek M, Kale C. Techno-economical evaluation of a hydrogen refuelling station powered by Wind-PV hybrid power system: A case study for Izmir-Cesme. Int J Hydrogen Energy 2018;43:10615–25.
[17] Bicer Y, Dincer I. Development of a new solar and geothermal based combined system for hydrogen production. Sol Energy 2016;127:269–84.
[18] Lummen N, Karouach A, Tveitan S. Thermo-economic study of waste heat recovery from condensing steam for hydrogen production by PEM electrolysis. Energy Convers Manage 2019;185:21–34.
[19] Nami H, Mohammadkhani F, Ranjbar F. Utilization of waste heat from GTMHR for hydrogen generation via combination of organic Rankine cycles and PEM electrolysis. Energy Convers Manage 2016;127:589–98.
[20] Feili M, Rostamzadeh H, Parikhani T, Ghaebi H. Hydrogen extraction from a new integrated trigeneration system working with zeotropic mixture, using waste heat of a marine diesel engine. Int J Hydrogen Energy 2020;45:21969–94.
[21] Thiyagarajan S, Sonthalia A, Geo VE, Chokkalingam B. Effect of waste exhaust heat on hydrogen production and its utilization in CI engine. Int J Hydrogen Energy 2020;45:5987–96.
[22] Arslan O. Performance analysis of a novel heat recovery system with hydrogen production designed for the improvement of boiler effectiveness. Int J Hydrogen Energy 2021;46:7558–72.
[23] Shaofu M, Hussein E, Hani B, Tao H, Xu Q. Exergy, economic, and optimization of a clean hydrogen production system using waste heat of a steel production factory. Int J Hydrogen Energy 2021 (article in press).
[24] Jamali DH, Noorpoor A. Optimization of a novel solar-based multi-generation system for waste heat recovery in a cement plant. J Cleaner Prod 2019;240:117825.
[25] Smolinka T, Ojong ET, Garche J. Hydrogen Production from Renewable Energies-Electrolyzer Technologies. In: Moseley PY, Garche J, editors. Electrochemical Energy Storage for Renewable Sources and Grid Balancing. Elsevier B.V; 2015. p. 103–28.
[26] Petibas F, Brisse A, Bouallou C. Benefits of external heat sources for high temperature electrolyzer systems. Int J Hydrogen Energy 2014;39:5505–13.
[27] Zhao Y, Xue H, Jin X, Xiong B, Liu R, Peng Y, et al. System level heat integration and efficiency analysis of hydrogen production process based on solid oxide electrolysis cells. Int J Hydrogen Energy 2021;46:38163–74.
[28] Seyitoglu SS, Dincer I, Kilicarslan A. Energy and exergy analyses of hydrogen production by coal gasification. Int J Hydrogen Energy 2017;42:2592–600.
[29] Wang F, Wang L, Zhang H, Xia L, Miao H, Yuan J. Design and optimization of hydrogen production by solid oxide electrolyzer with marine engine waste heat recovery and ORC cycle. Energy Convers Manage 2021;229:113775.
[30] Toklu E, Avci AC, Kaygusuz K, Gur M. A research on hydrogen production from industrial waste heat by thermal water splitting. Int J Hydrogen Energy 2016;41:10071–9.
[31] Kowalczyk T, Badur J, Bryk M. Energy and exergy analysis of hydrogen production combined with electric energy generation in a nuclear cogeneration cycle. Energy Convers Manage 2019;198:111805.
[32] Balta MT, Kizilkan O, Yılmaz F. Energy and exergy analyses of integrated hydrogen production system using high temperature steam electrolysis. Int J Hydrogen Energy 2016;41:8032–41.
[33] M. Mehrpooya F.K. Bahnamiri S.M. Moosavian SMA. Energy analysis and economic evaluation of a new developed integrated process configuration to produce power, hydrogen, and heat Journal of Cleaner Production 2019 118042.
[34] Ishaq H, Dincer I, Naterer GF. Exergy and cost analyses of waste heat recovery from furnace cement slag for clean hydrogen production. Energy 2019;172:1243–53.
[35] Wang F, Wang L, Ou Y, Lei X, Yuan J, Liu X, et al. Thermodynamic analysis of solid oxide electrolyzer integration with engine waste heat recovery for hydrogen production. Case Studies in Thermal Engineering 2021;27:101240.
[36] H. Zhang L. Wang M. Pérez-Fortes Van herle J, Maréchal F, Umberto D. Techno-economic optimization of biomass-to-methanol with solid-oxide electrolyzer Applied Energy 258 2020 114071.
[37] Hosseini SE. Design and analysis of renewable hydrogen production from biogas by integrating a gas turbine system and a solid oxide steam electrolyzer. Energy Convers Manage 2020;211:112760.
[38] Arslan O. The first and second law analysis of Seyitomer coal-fired power plant. Turkey: Dumlupinar University; 2005.
[39] Arslan O, Kose R. The first and second law analysis of Seyitomer coal - fired power plant. Journal of Science and Technology of Dumlupinar University 2005;8:87–106.
[40] Arslan O, Kilic D. Concurrent optimization and 4E analysis of organic Rankine cycle power plant driven by parabolic trough collector for low-solar radiation zone. Sustainable Energy Technol Assess 2021;46:101230.
[41] Bejan A, Tsatsaronis G, Moran M. Thermal Design and Optimization. New York: John Wiley & Sons Inc.; 1996.
[42] Arslan O, Acar MS. Enhanced Exergetic Evaluation of Regenerative and Recuperative Coal-Fired Power Plant. Int J Exergy 2021;35:263–89.
[43] Acar MS, Saraydar M, Arslan O. Exergetical evaluation of lignite production process: SLI case study. Journal of Polytechnic 2018;21:55–63.
[44] Cengel YA, Boles MA. Thermodynamics: An Engineering Approach. New York: McGraw Hill Inc., USA; 1994.
[45] Arslan O, Ozgur MA, Yildizay HD, Kose R. Fuel Effects on Optimum Insulation Thickness: An Exergetic Approach. Energy Sources Part A 2010;32:128–47.
[46] Avşar A, Arslan O. Thermodynamic Analysis of the Heating Concept for a Residence. BSEU Journal of Science 2020;7:80–90. https://doi.org/10.35193/bseufbd.706281.
[47] Ucar M, Arslan O. Assessment of improvement potential of a condensed combi boiler via advanced exergy analysis. Thermal Science and Engineering Progress 2021;23:100853.
[48] Strehlow RA. Combustion Fundamentals. Energy, Combustion and Environment Series. Singapore: McGraw Hill Inc., Singapore, 1984.
[49] Arslan O, Yetik O. ANN based optimization of supercritical ORC-Binary geothermal power plant: Simav case study. Appl Therm Eng 2011;31(17–18):3922–8.
[50] Arslan O, Ozgur MA, Kose R. Electricity generation ability of the Simav geothermal field: A technoeconomic approach. Energy Sources Part A 2012;34(12):1130–44.
[51] Refprop. Reference Fluid Thermodynamics and Transport Properties. NIST Reference Database, Version 9.0. National Institute of Standards. NIST, USA: and Technology; 2010.
[52] Wypych G. Handbook of Foaming and Blowing Agents. Canada: ChemTec Publishing; 2017.
[53] Smolinka T, Ojong ET, Garche J. Hydrogen Production from Renewable Energies-Electrolyzer Technologies. In: Moseley PT, Garche J, editors. Electrochemical Energy Storage for Renewable Sources and Grid Balancing. Elsevier, 2015.
[54] Ni M, Leung MKH, Leung DYC. Parametric study of solid oxide steam electrolyzer for hydrogen production. Int J Hydrogen Energy 2007;32:2305–13.
[55] Pacheco EH, Singh D, Hutton PN, Patel N, Mann MD. Macro-level model for determining the performance characteristics of solid oxide fuel cells. J Power Sources 2004;138:174–86.
[56] Hosseini SE. Performance evaluation of a solarized gas turbine system integrated to a high temperature electrolyzer for hydrogen production. Int J Hydrogen Energy 2020;45:21068–86.
[57] Choi PH, Bessarabov DG, Datta R. A simple model for solid polymer electrolyte (SPE) water electrolysis. Solid State Ionics 2004;175:535–9.

[58] Ni M, Leung MKH, Leung DYC. A modeling study on concentration overpotentials of a reversible solid oxide fuel cell. J Power Sources 2006;163:460–6.
[59] Visitdumrongkul N, Tippawan P, Authayanun S, Assabumrungrat S, Arpornwichanop A. Enhanced performance of solid oxide electrolysis cells by integration with a partial oxidation reactor: Energy and exergy analyses. Energy Convers Manage 2016;129:189–99.
[60] Ferguson JR, Fiard JM, Herbin R. Three-dimensional numerical simulation for various geometries of solid oxide fuel cells. J Power Sources 1996;58:109–22.
[61] Ebbesen SD, Graves C, Mogensen M. Production of synthetic fuels by co-electrolysis of steam and carbon dioxide. Int J Green Energy 2009;6:646–60.
[62] Arslan O. ANN-based determination of optimum working conditions of residential combustors with respect to optimum insulation. Energy Sources Part A 2014;36:2603–12.
[63] Tugcu A, Arslan O. Optimization of geothermal energy aided absorption refrigeration system—GAARS: A novel ANN-based approach. Geothermics 2017;65:210–21.
[64] Arat H, Arslan O. Optimization of district heating system aided by geothermal heat pump: A novel multistage with multilevel ANN modeling. Appl Therm Eng 2017;111:608–23.
[65] AlZahrani AA, Dincer I. Thermodynamic and electrochemical analyses of a solid oxide electrolyzer for hydrogen production. Int J Hydrogen Energy 2017;42:21404–13.